Tecnociencia, Vol. 28, N°1: 38-71
Enero-Junio 2026
ISSN L 2415-0940

Spectroscopic analysis and modeling of quasar 3C-279

Análisis espectroscópico y modelado del cuásar 3C-279

Franklin Vasquez Guardia
Dipartimento di Fisica e Astronomia "Galileo Galilei", Università degli Studi di Padova, Vicolo dell'Osservatorio 3, I-35122, Padova, Italia.
franklinsimon.vasquezguardia@studenti.unipd.it https://orcid.org/0000-0002-1413-6617

Fecha de recepción: 1 de octubre de 2025
Fecha de aceptación: 23 de octubre de 2025

DOI: https://doi.org/10.48204/j.tecno.v28n1.a8945

ABSTRACT

We analyze the X-ray and ultraviolet emission of the AGN 3C-279 using Swift data. Located 5 billion light-years away at a redshift distance of Z=0.537, 3C-279 is a bright AGN powered by a relativistic jet from its supermassive black hole and served as a calibration source for the EHT's first black hole image.

We model the spectral emission of 3C-279 in the 0.3–6 keV range to study its luminosity evolution before, during, and after a GRB event, comparing our results with those in the previous literature. Five Swift datasets were processed with HEASARC software, using XRT and UVOT data to characterize X-ray and UV behavior. The results confirm expected luminosity peaks and flare activity, consistent with published studies, demonstrating the capability of XRT and UVOT to probe low- to mid-energy X-ray and UV phenomena.

KEYWORDS

Active Galactic Nucleus, Aperture Photometry, Spectral Analysis, Light curve

RESUMEN

Analizamos la emisión en rayos X y ultravioleta del AGN 3C-279 utilizando datos del satélite Swift. Ubicado a 5 mil millones de años luz a una distancia redshift de Z=0.537, 3C-279 es un núcleo galáctico activo brillante alimentado por un haz relativista de su agujero negro supermasivo y fue una fuente de calibración para la primera imagen de un agujero negro obtenida por el EHT.

Se modeló la emisión espectral de 3C-279 en el rango de 0,3 a 6 keV para estudiar su evolución de luminosidad antes, durante y después de un evento de estallido de rayos gamma GRB, comparando los resultados con la literatura existente. Se analizaron cinco conjuntos de datos de Swift, procesados con software de HEASARC, empleando datos de XRT y UVOT para caracterizar su comportamiento en rayos X y UV. Los resultados confirman los picos de luminosidad y la actividad de llamaradas esperados, demostrando la eficacia de XRT y UVOT para estudiar fenómenos astrofísicos en los rangos bajo y medio de energía.

PALABRAS CLAVE

Núcleo Activo de Galaxia, Fotometría de Apertura, Análisis Espectral, Curva de Luz

INTRODUCCIÓN

The target for our data analysis is the blazar 3C-279, located at $\alpha = 12^{h}\,56^{m}\,11.7^{s}, \delta = -05^{h}\,47^{m}\,21.6^{s}$ (JD 2000.0) and at a distance of Z = 0.537 (3.08 Gpc ≈ 5 Gly) from Earth. It is powered by a supermassive black hole and exhibits intense gamma-ray variability, rapid flares, and emission across multiple wavelengths. It was the first blazar to be observed in gamma rays (Hartman et al., 1992)

A blazar is a subtype of active galactic nucleus (AGN) where the relativistic jet is pointed almost directly toward the solar system. As a result, the galactic engine can be observed more easily and appears more luminous than it would otherwise be when viewed from the side (Rajguru 2010; 2024).

Previous observations of 3C-279 have shown that the blazar experiences surges in activity lasting days, which some propose to be cyclic (Wang 2022; Hayashida 2015), separated by longer periods of stable activity lasting months or years. These surges are characterized by bursts of energy, especially in gamma rays, with reported flares in 2012 (Blinov 2021), 2015 (Singh 2020), and 2017–2018 (Prince 2020). This makes 3C-279 an ideal candidate to study the relationship between supermassive black holes and their environments and, in our case, to analyze how the flux over a certain energy range behaves during different activity states.

Figure 1.
Artistic representation of Quasar 3C-279 from scientific data (ESO 2012).

Most of the energetic flux in an AGN is primarily generated by the supermassive black hole at its center and the surrounding accretion disk formed by infalling matter (Epstein & Martin 2025). In a typical AGN, the central black hole is not isolated from its environment but surrounded by enormous quantities of matter. This matter does not fall directly into the black hole but instead accretes as it spins and is drawn toward the center (Bellovary, 2016).

This accretion process can heat the gas to temperatures of millions of degrees, producing bolometric luminosities on the order of $10^{46} - 10^{48}\ erg/s$, comparable to the total energy output of entire galaxies. Additionally, friction and twisting magnetic fields enhance the chaotic activity near the black hole (Alston, 2022). If enough gravitational energy is converted into heat, a relativistic jet of highly energetic particles, such as electrons and ions, is emitted from the poles of the rotating black hole, and the AGN is classified as a quasar (Fabian 2012). If this beam is pointed toward Earth, an even higher apparent luminosity can be detected, and the object is recognized as a blazar.

AGNs typically emit radiation across the entire electromagnetic spectrum (Padovani 2023), though not all of it is detectable due to absorption by the galactic disk, intergalactic dust, high redshift, or instrument sensitivity limits.

INSTRUMENTATION

For this research, we used several datasets of 3C-279 observed with the Swift telescope. Swift is a space observatory launched in 2004 by NASA to detect and study gamma-ray bursts (GRBs). It carries three instruments: BAT (Burst Alert Telescope), XRT (X-ray Telescope), and UVOT (Ultraviolet/Optical Telescope), which together enable rapid multi-wavelength follow-up observations (Swift Team 2025)

The Burst Alert Telescope (BAT)

BAT is Swift's primary instrument, designed to detect and locate GRBs in real time and determine their sky coordinates. It then triggers the spacecraft to reorient the XRT and UVOT instruments. It also provides hard X-ray imaging of transient events, with an energy detection range of 15–150 keV, a 1.4 steradian field of view (≈ 16% of the sky), and a CdZnTe detector array of 32,768 elements (total area ≈ 5 200 cm^2).

The X-ray Telescope (XRT)

XRT provides precise localization and time-resolved spectroscopy of X-ray afterglows of GRBs. It has an energy coverage of 0.2–10 keV (soft to medium X-rays), an effective area of approximately 110 cm^2 at 1.5 keV, and a field of view of 23.6 × 23.6 arcmin (Burrows et al., 2005).

XRT operates in three modes:

- Photon Counting (PC): low count rate, full CCD imaging in 2.5 s intervals.
- Windowed Timing (WT): high count rate, 1D imaging of a 200 × 100 pixel strip at 1.8 ms intervals.
- Piled up Mode: handles bright sources that saturates the others.

The UV/Optical Telescope (UVOT)

UVOT provides rapid optical and ultraviolet follow-up observations of GRBs detected by Swift. It covers 170–650 nm (UV to optical), with a 30 cm aperture and 17 × 17 arcmin field of view. It includes six broad-band filters (V, B, U, UVW1, UVM2, UVW2), a white filter, grism, and magnifier.

Typical 5σ sensitivities at 1000 s exposure are:

Table 1.
UVOT filter response and sensitivity (at 5σ, 1000 s exposure) (Swift UVOT Filters).

Filter	Central Wavelength (Å)	Magnitude (AB)
V	5468	22.3
B	4392	22.3
U	3465	22.7
UVW1	2600	21.7
UVM2	2246	20.7
UVW2	1928	21.3

Software

The main software used was NASA's HEASARC HEASoft package, which includes FTOOLS and XANADU.

- XANADU : high-level, multi-mission tools for spectral, timing, and imaging analysis.
- FTOOLS: general and mission-specific tools for manipulating FITS files.
  Additional utilities include:
- FITSIO (core library for reading/writing FITS files),
- fv (FITS browser/editor/plotter),
- XSTAR (for modeling photoionized gases).
  SAOImage DS9 was also used for visualization and to define apertures for photometry.

Datasets

The datasets were obtained from the HEASARC database (HEASARC 2025). Two main criteria guided selection:

(1) a long, continuous observing window; and (2) a small offset from the target.
The first dataset (obsID 00035019011) met these requirements with a duration of 15 483 s (≈ 4.3 h) and offset of 0.3 arcmin. For the GRB flare reported by Singh (2020) on June 16, 2015 (J2000, UTC), we retrieved datasets 00035019180 and 00035019181. To complement the

analysis, we also included pre- and post-event observations in the 00035019176 and 00035019185 datasets.

Table 2.
Swift datasets used in this research.

ObsID	Date	Start (UTC)	XRT Duration (s)	UVOT Duration (s)
00035019011	30/11/2008	00:22:00	15 483.46	15 574.77
00035019176	15/06/2015	14:27:58	1995.81	1994.11
00035019180	16/06/2015	03:27:59	962.87	961.70
00035019181	16/06/2015	16:04:58	937.70	936.10
00035019185	17/06/2015	20:59:58	491.44	488.56

METHODOLOGY AND DATA PROCESSING

Each dataset contains files for UVOT, XRT, and BAT instruments. This analysis focuses on UVOT and XRT.

UVOT Data Processing

From the subset of files corresponding to the UVOT instrument, the image files with the "_sk" suffix were selected, indicating frames that contain sky coordinates, i.e., right ascension (α) and declination (δ).

The images were visually inspected using "DS9" software to confirm that the target was within the field of view and free from contaminants such as blurring or data artifacts that could render the data unusable. Each image was also checked for aspect correction to account for possible offsets between frames, as a single "_sk" image file may include multiple exposures. When aspect correction was available, the images were co-added to improve the signal-to-noise ratio (S/N). After merging, aperture photometry was performed on the co-added image. This technique measures the flux of the target by selecting a circular or elliptical aperture around the object and subtracting the flux from a surrounding background aperture that contains no other sources as seen on Figure 2.
HEASoft provides two methods for analyzing sources in UVOT images: an automatic detection mode for aperture photometry and a manual mode in which the user defines the coordinates, aperture size, and shape. For this analysis, the manual mode was selected.

For all datasets, a 5-pixel aperture was used for the source and a 20-pixel aperture for the background. These values were determined through visual inspection in DS9 to minimize contamination from nearby sources. The photometric analysis was performed using the "uvotsource" command and obtained plots and images can be seen on the Results section.

A Lightcurve and a spectral plot were generated from the aperture photometry data. The number of lightcurve data points varies between datasets, while each spectral plot contains a single data point per dataset due to the telescope's operational configuration. This is explained in greater detail in the Discussion section.

Figure 2.
Left: UVOT field of view for obsID 00035019011. Right: target region with 5 and 20 arcsec aperture rings.

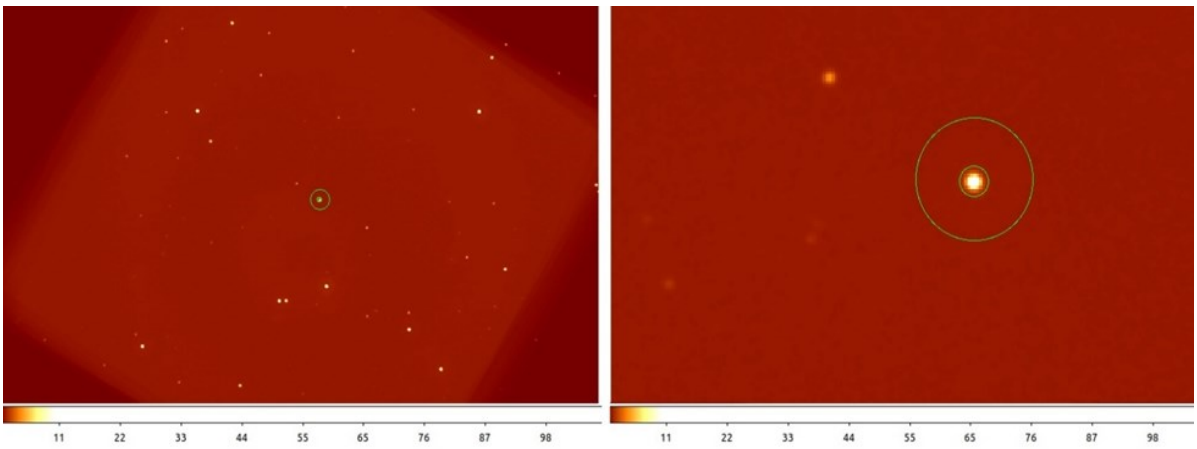

XRT Data Processing
For the XRT data reduction, event files generated onboard the telescope were used, specifically those obtained when the telescope operated in Photon Counting (PC) mode. In this configuration, the full CCD frame is exposed, allowing complete spatial and spectral information to be analyzed.

The data were processed using the xrtpipeline, which automates data calibration and filtering. The input parameters include the target coordinates in right ascension (α) and declination (δ). By default, the pipeline extracts a circular region of 20 pixels (approximately 47 arcseconds) around the target. This default value was considered appropriate, as the analysis focused on energy levels up to 10 keV. According to Burrows et al. (2005) and the Swift XRT technical

documentation (NASA), approximately 90% of the Point Spread Function (PSF) is contained within a radius of about 30 arcseconds for these energy levels.

Figure 3 shows the XRT field of view for observation ID 00035019011, including the detected target and the coordinate grid.

The pipeline produces three output files: a spectrum file (.pha), a lightcurve file (.lc), and an image file (.img), as illustrated in Figure 3. The lightcurve and spectrum files were further processed separately, and their corresponding plots and analyses are presented in the Results section.

Lightcurves were produced using the “lcurve” command. Since the original lightcurves are often recorded with very short time resolutions (small bin sizes), a large number of data points may be produced. Rebinning was therefore applied, especially for long exposures or bright sources. The lcurve command allows the user to specify bin durations, determining the counts accumulated in each time bin. The binning parameters and the statistical values for each dataset are presented in the Results section.

The spectral files (.pha) were calibrated using two auxiliary files: the Response Matrix File (RMF), which converts raw counts into physical quantities such as flux and spectral parameters, and the Ancillary Response File (ARF), which describes the telescope’s effective area as a function of energy and time. Both file types are provided by the CALDB calibration database included in the HEASoft package and were applied using the “grppha” command.

Spectral analysis was carried out using the XSPEC X-ray fitting package. Before fitting, the data were inspected for channels flagged as having poor quality, typically due to a low number of counts in a given energy bin. The grppha command was also used to group the data, ensuring at least 20 counts per channel so that Gaussian statistics could be applied.

The final spectral plots were generated by excluding energy ranges outside the XRT sensitivity (below 0.3 keV and above 10.2 keV) and removing flagged channels. The resulting spectra for each dataset are shown in Figure 8.

Figure 4 shows an example spectrum from observation 00035019011, including all channels within the XRT sensitivity range.

Figure 3.
XRT detected target source and field of view for obsID 00035019011.

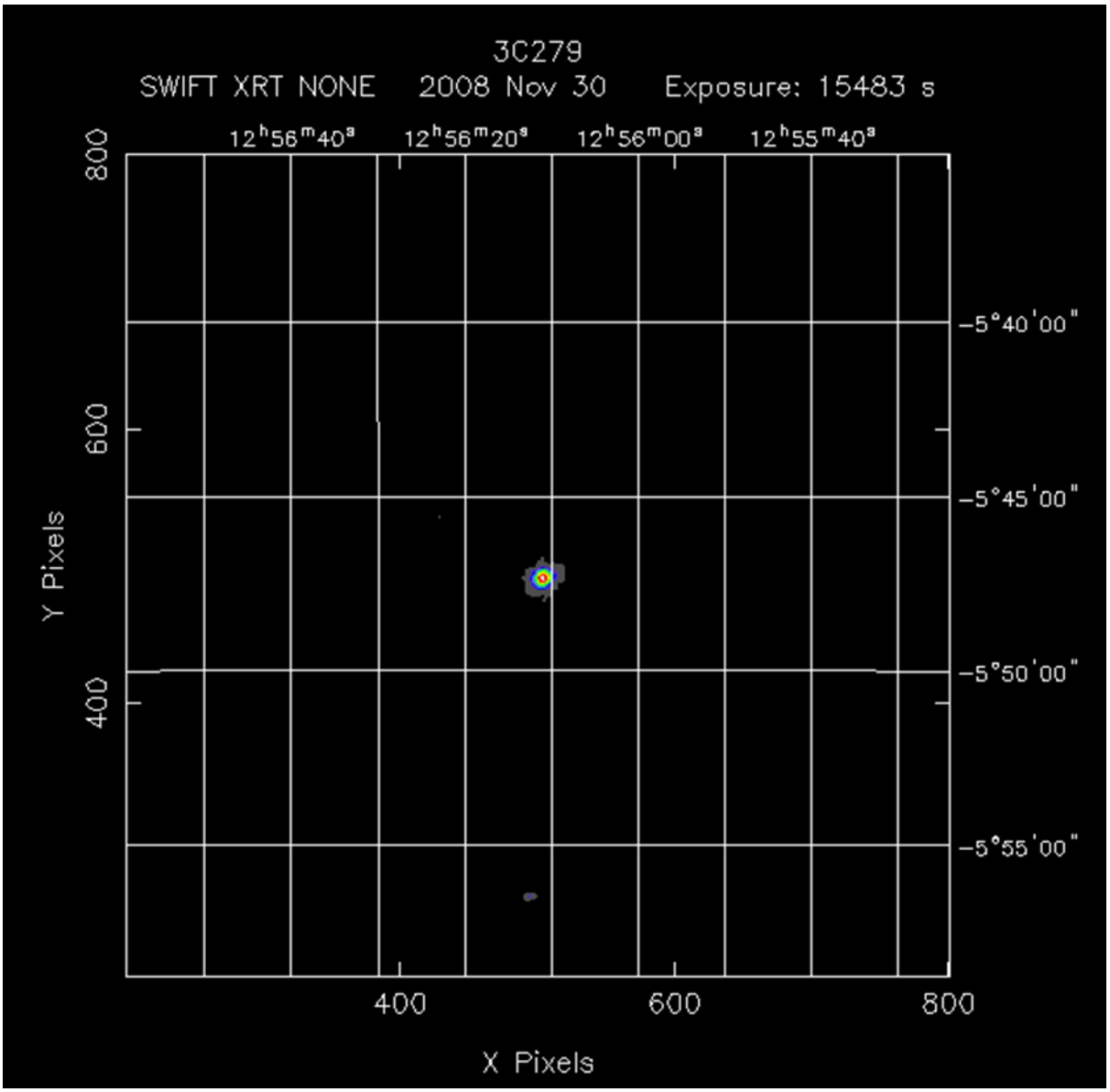

Figure 4.
Spectrum of obsID 00035019011 with all channels within XRT sensitivity range included.

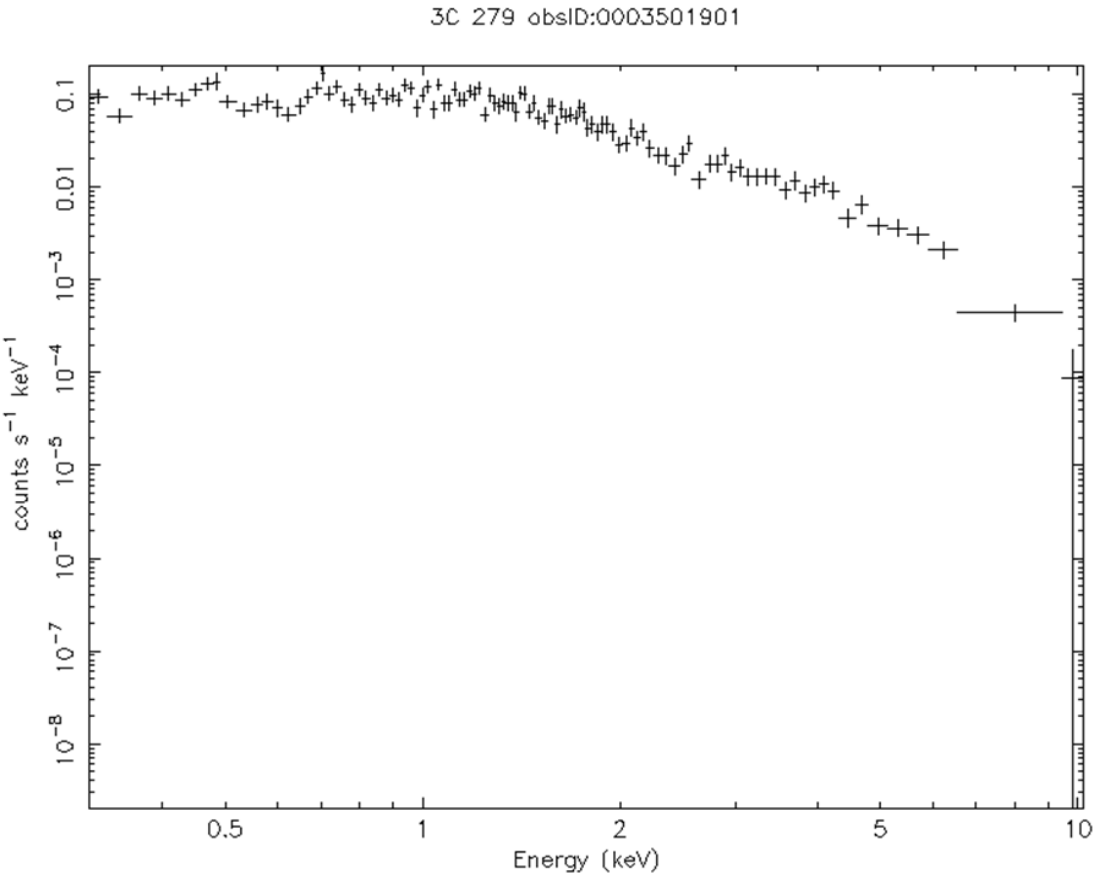

Model Fitting

We then proceeded to fit the data with a model. XSPEC allows for different types of models, with multiplicative and additive being the basic types, and it also allows combining them.

By looking at our spectrum plots, especially before removing the flagged channels (Figure 4), we see that the data appear to follow a power law, quite different from the thermal emission characteristic of a stellar spectrum. Therefore, we chose a power-law model to fit our data, described by:

$$A(E) = KE^{-\alpha}$$

- A represents the additive component,
- α is the photon index of the power law,
- K represents the normalization constant in units of photons keV^{-1} cm^{-2} s^{-1} at 1 keV.

Taking into consideration the reported distance of $Z = 0.537$ to our source 3C-279, we also included the absorption of the flux due to extinction, which refers to how much of the flux from the source has been absorbed by matter before reaching the detector. Since neutral hydrogen is commonly present in interstellar dust and gas, we include a hydrogen column density between the source and the telescope, expressed as N_H (cm^{-2}), to account for absorption.

With the model "phabs*,"* we take this absorption into account. This model has the form:

$$M(E) = exp[-N_H\,\sigma(E)\,]$$

- M represents the multiplicative component of the model,
- N_H represents the galactic extinction,
- $\sigma(E)$ is the photoelectric cross-section.

To start the fitting, the command "model" allows us to input the chosen model and evaluate how well it fits the data. In our case, the command takes the form "model phabs(powerlaw)." The program takes three inputs for this model: the hydrogen column density N_H $(cm^{-2})\rangle$, the photon index α, and the normalization constant K (photons keV^{-1} cm^{-2} s^{-1} at 1 keV).

The magnitude of the extinction is obtained from the "nh" command, another tool provided by XSPEC. This package simulates the attenuation of X-ray (or other electromagnetic) photons as they pass through interstellar hydrogen gas along the line of sight of the target. For 3C-279, we obtained an average value of $0.022 \times 10^{-22}\ cm^{-2}$ for the hydrogen column density.

Several authors (Albert 2008); (Singh 2020); (Thekkoth 2023) report a power index of approximately 2 for the energy ranges in which XRT provides reliable precision (0.3–10 keV). Therefore, we adopted a value of 2 for the power index as the model input.

The normalization factor was estimated by measuring the counts s^{-1} around the 1 keV energy level and dividing by the effective area of XRT $(135\ cm^2)$.

We then froze the parameter N_H, since we consider it a reliable estimate for the hydrogen column density and wish to evaluate how well the model fits our data with this fixed value. The model was subsequently re-normalized and fitted to the data.

We used the command “error” to check the 90 % confidence level for our parameters, and performed a goodness test on the fit, as seen in the results and discussion sections.

To include the emitted flux in our model, we added an additional term with the command “editmod phabs × cflux(powerlaw),” where we specify the energy ranges for the flux to be measured. We selected the 0.3–6 keV range for all datasets, as explained in the Discussion.

We ended up with six variables in the model, of which four were fixed: the hydrogen column density, the minimum and maximum flux magnitudes, and the normalization factor (also fixed for reference). We then re-evaluated the 90 % confidence range for the free parameters. Finally, our model allowed us to calculate the flux emitted from the source between 0.3 and 6 keV, as shown in the following section.

RESULTS

UVOT Results

For all UVOT datasets where aperture photometry was performed, we present the resulting lightcurve plots in Figure 5 and tables containing the Magnitude measured in both the AB and Vega systems in Tables 3 to 8. Spectrum plots are also presented in Figure 6. It must be mentioned that the dataset from obsID:00035019181 (see Table 2) did not produce lightcurve or spectrum plots; this is further touched upon in the Discussion. On the other hand, from the dataset of obsID:00035019011 (see Table 2), we were able to extract two lightcurve and spectrum plots, one for each of the filters used on this dataset (U and UVW2).

Table 3.
UVOT source analysis for obsID 00035019011 (U Filter)

U Filter	Source	Background [arcsec^{-2}]	Background Limit	Coincidence Limit
Significance (σ)	427,1	5	–	–
Magnitude (Vega System)	15,25 ± 0.02 [stat] ± 0.02 [sys]	21,57	20,78	11,91
Magnitude (AB System)	16,27 ± 0,02 [stat] ± 0,02 [sys]	22,59	21,80	12,93
Flux Density [erg s^{-1} cm^{-2} Å^{-1}]	(2,81 ± 0,06 [stat] ± 0,09 [sys]) × 10^{-15}	(8,33 ± 0,01 [stat] ± 0,13 [sys]) × 10^{-18}	1,72 × 10^{-17}	6,06 × 10^{-14}

Table 4.
UVOT source analysis for obsID 00035019011 (UVW2 Filter)

UVW2 Filter	Source	Background [arcsec^{-2}]	Background Limit	Coincidence Limit
Significance (σ)	97,8	5	–	–
Magnitude (Vega System)	15,64 ± 0.02 [stat] ± 0.03 [sys]	23,58	19,57	10,95
Magnitude (AB System)	17,37 ± 0,02 [stat] ± 0,03 [sys]	25,31	21,70	12,68
Flux Density [erg s^{-1} cm^{-2} Å^{-1}]	(2,96 ± 0,05 [stat] ± 0,06 [sys]) × 10^{-15}	(1,97 ± 0,02 [stat] ± 0,4 [sys]) × 10^{-18}	5,52 × 10^{-17}	2,22 × 10^{-14}

Table 5.
UVOT source analysis for obsID 00035019176 (U Filter)

U Filter	Source	Background [arcsec^{-2}]	Background Limit	Coincidence Limit
Significance (σ)	205,2	5	–	–
Magnitude (Vega System)	14,93 ± 0.02 [stat] ± 0.02 [sys]	22,88	20,26	11,91
Magnitude (AB System)	15,95 ± 0,02 [stat] ± 0,02 [sys]	23,90	21,28	12,93
Flux Density [erg s^{-1} cm^{-2} Å^{-1}]	(3,77 ± 0,08 [stat] ± 0,06 [sys]) × 10^{-15}	(2,49 ± 0,01 [stat] ± 0,04 [sys]) × 10^{-18}	2,77 × 10^{-17}	6,06 × 10^{-14}

Table 6.
UVOT source analysis for obsID 00035019180 (UVW2 Filter)

UVW2 Filter	Source	Background [arcsec⁻²]	Background Limit	Coincidence Limit
Significance (σ)	74,1	5	–	–
Magnitude (Vega System)	15,22 ± 0.03 [stat] ± 0.03 [sys]	24,33	19,89	10,95
Magnitude (AB System)	16,95 ± 0,03 [stat] ± 0,03 [sys]	26,06	21,62	12,68
Flux Density [erg s^{-1} cm^{-2} $Å^{-1}$]	(4,83 ± 0,10 [stat] ± 0,10 [sys]) × 10^{-15}	(9.92 ± 0,23 [stat] ± 0,22 [sys]) × 10^{-19}	5,91 × 10^{-17}	2,22 × 10^{-13}

Table 7.
UVOT source analysis for obsID 00035019181 (UVW2 Filter)

UVW2 Filter	Source	Background [arcsec⁻²]	Background Limit	Coincidence Limit
Significance (σ)	70,1	5	–	–
Magnitude (Vega System)	15,30 ± 0,03 [stat] ± 0,03 [sys]	24,33	19,88	10,95
Magnitude (AB System)	17,03 ± 0,03 [stat] ± 0,03 [sys]	26,06	21,61	12,68
Flux Density [erg s^{-1} cm^{-2} $Å^{-1}$]	(4,04 ± 0,10 [stat] ± 0,09 [sys]) × 10^{-15}	(9.91 ± 0,23 [stat] ± 0,22 [sys]) × 10^{-19}	5,99 × 10^{-17}	2,22 × 10^{-13}

Table 8.
UVOT source analysis for obsID 00035019185 (UVM2 Filter)

UVM2 Filter	Source	Background [arcsec^{-2}]	Background Limit	Coincidence Limit
Significance (σ)	55,7	5	–	–
Magnitude (Vega System)	15,32 ± 0,03 [stat] ± 0,03 [sys]	24,02	19,51	10,42
Magnitude (AB System)	17,01 ± 0,03 [stat] ± 0,03 [sys]	25,71	21,20	12,11
Flux Density [erg s^{-1} cm^{-2} Å^{-1}]	(3,45 ± 0,10 [stat] ± 0,02 [sys]) × 10^{-15}	(1,14 ± 0,03 [stat] ± 0,01 [sys]) × 10^{-18}	7,29 × 10^{-17}	3,14 × 10^{-13}

Figure 5.
Lightcurves obtained from the UVOT data.

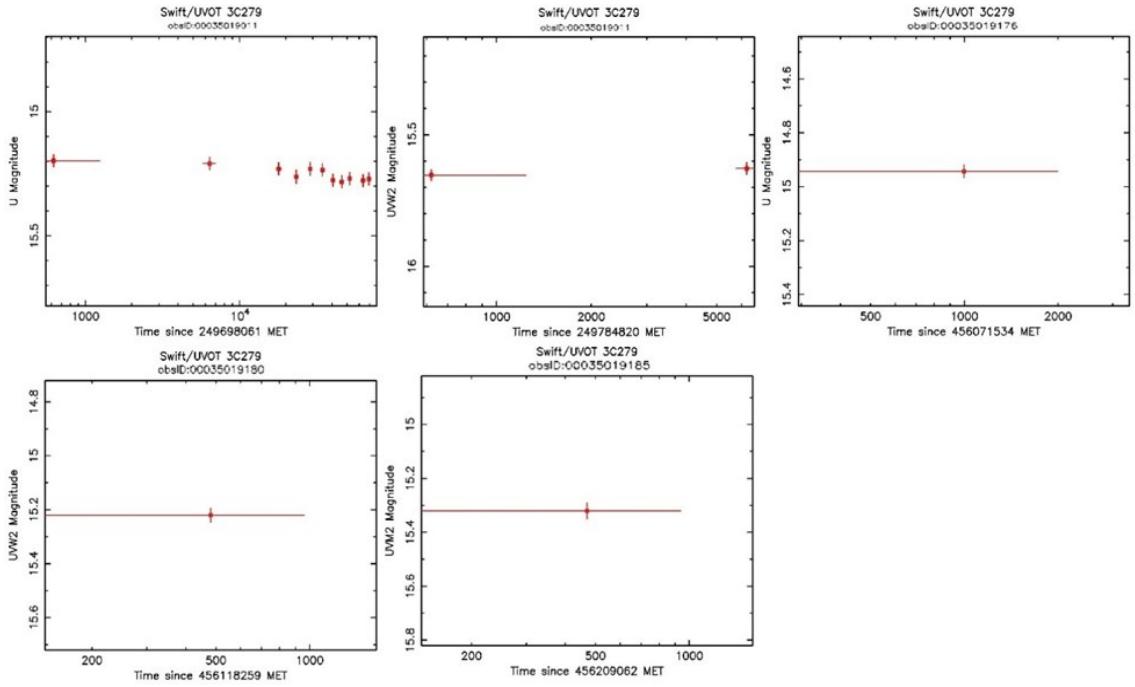

Figure 6.
Spectrum plots from UVOT data.

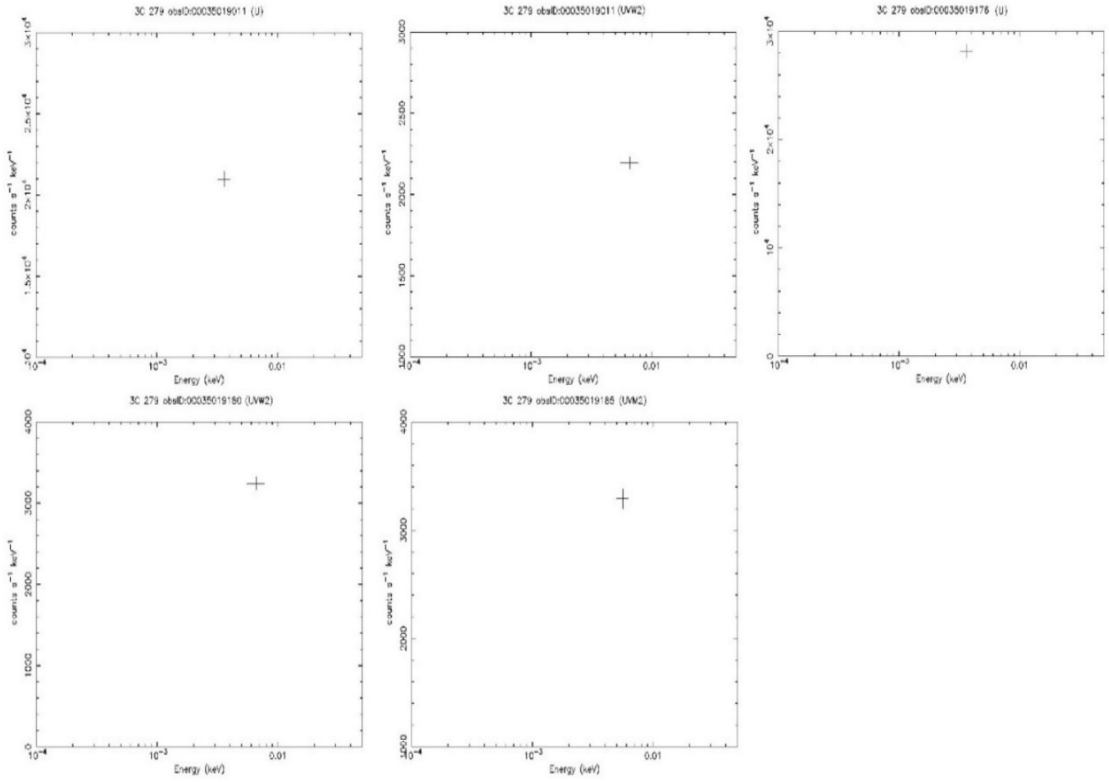

XRT Results

As described before, the XRT dataset analysis mainly focused on two files produced from the xrtpipeline: the lightcurve file, which plots counts/s vs time (Figure 7) and the spectrum file, which plots counts s^{-1} keV^{-1} vs energy (Figure 8)

Figure 7.
Lightcurves produced from all XRT observations

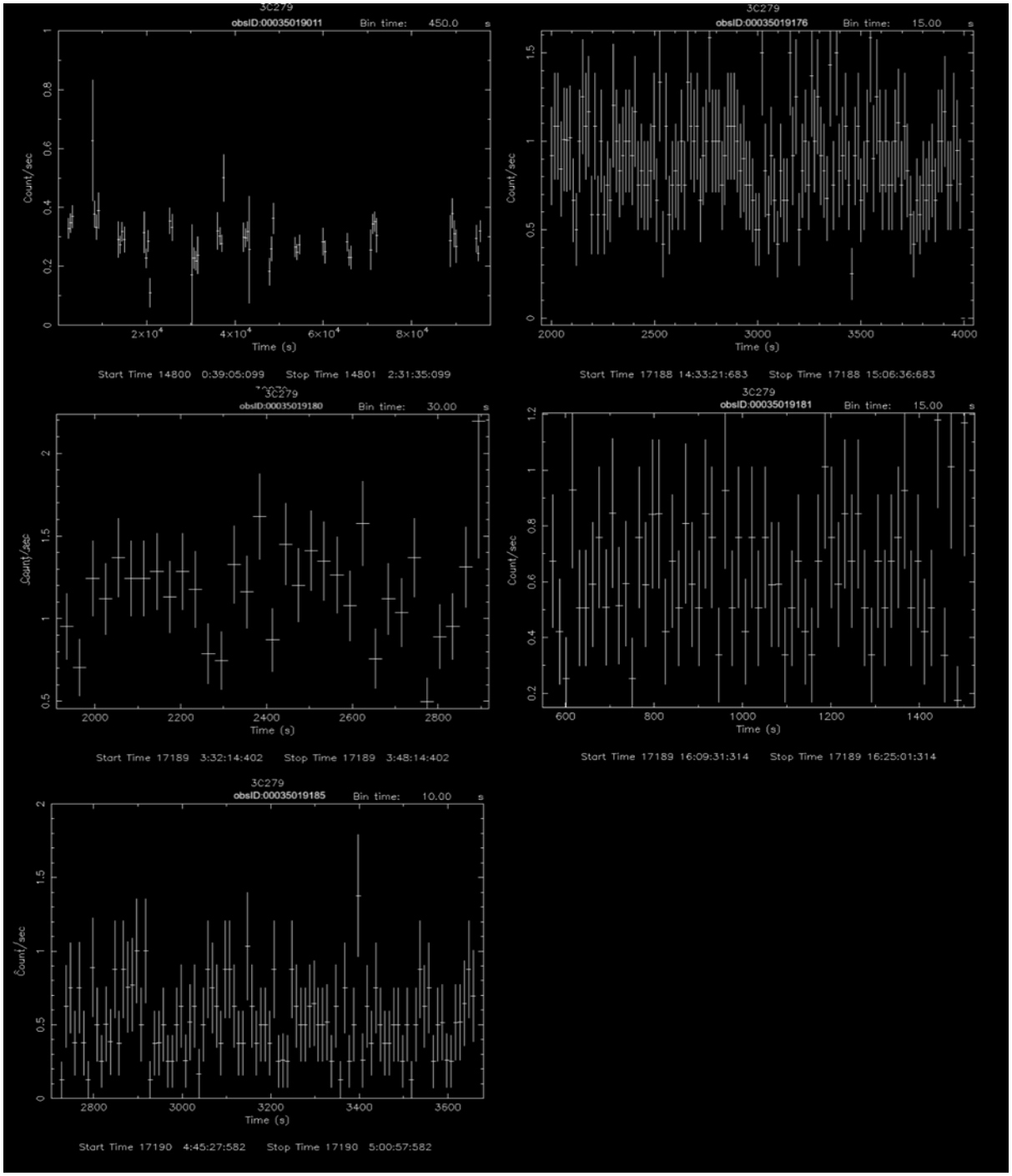

XRT Lightcurves

The lightcurve plots can be seen in Figure 8, and their respective statistical analysis in Tables 9 to 13.

Table 9.
Results from statistical analysis of X-ray spectrum lightcurve (obsID 00035019011)

Parameter	Obtained Value
Newbin Integration Time (s)	450.00
Interval Duration (s)	93150.00
No. of Newbins	51
Average (c/s)	0.29860 ± 0.90E-02
Standard Deviation (c/s)	0.77570E-01
Minimum (c/s)	0.11062
Maximum (c/s)	0.62750
Variance ((c/s)²)	0.60171E-02 ± 0.12E-02
Expected Variance ((c/s)²)	0.40254E-02 ± 0.81E-03
Third Moment ((c/s)³)	0.62264E-03
Average Deviation (c/s)	0.52517E-01
Skewness	1.4192 ± 0.34
Kurtosis	5.3714 ± 0.69
Chi-Square	40.046 dof 50
Chi-Square Prob of constancy	0.84192
Kolm.-Smir. Prob of constancy	0.62448E-07
RMS fractional variation	0.98076E-01 (3 sigma)

Table 10.
Results from statistical analysis of X-ray spectrum lightcurve (obsID 00035019176)

Parameter	Obtained Value
Newbin Integration Time (s)	15.00
Interval Duration (s)	2010.0
No. of Newbins	134
Average (c/s)	0.89252 ± 0.24E-01
Standard Deviation (c/s)	0.25959E-01
Minimum (c/s)	0.0000
Maximum (c/s)	1.5847
Variance ((c/s)^2)	0.67385E-01 ± 0.83E-02
Expected Variance ((c/s)^2)	0.74919E-01 ± 0.92E-02
Third Moment ((c/s)^3)	0.17928E-02
Average Deviation (c/s)	0.20322
Skewness	0.10249 ± 0.21
Kurtosis	0.87967 ± 0.42
Chi-Square	111.96 dof 133
Chi-Square Prob of constancy	0.90717
Kolm.-Smir. Prob of constancy	0.28731
RMS fractional variation	< 0.21877 (3 sigma)

Table 11.

Results from statistical analysis of X-ray spectrum lightcurve (obsID 00035019180)

Parameter	Obtained Value
Newbin Integration Time (s)	30.000
Interval Duration (s)	990.00
No. of Newbins	33
Average (c/s)	1.1733 ± 0.46E-01
Standard Deviation (c/s)	0.31209
Minimum (c/s)	0.49750
Maximum (c/s)	2.1943
Variance ((c/s)^2)	0.97400E-01 ± 0.24E-01
Expected Variance ((c/s)^2)	0.67122E-01 ± 0.17E-01
Third Moment ((c/s)^3)	0.17040E-01
Average Deviation (c/s)	0.22977
Skewness	0.58691 ± 0.43
Kurtosis	1.8792 ± 0.85
Chi-Square	34.723 dof 32
Chi-Square Prob of constancy	0.33947
Kolm.-Smir. Prob of constancy	0.82356E-01
RMS fractional variation	< 0.15088 (3 sigma)

Table 12.

Results from statistical analysis of X-ray spectrum lightcurve (obsID 00035019181)

Parameter	Obtained Value
Newbin Integration Time (s)	15.000
Interval Duration (s)	945.00
No. of Newbins	63
Average (c/s)	0.6928 ± 0.30E-01
Standard Deviation (c/s)	0.21638
Minimum (c/s)	0.17420
Maximum (c/s)	1.1795
Variance ((c/s)^2)	0.46820E-01 ± 0.84E-02
Expected Variance ((c/s)^2)	0.55380E-01 ± 0.99E-02
Third Moment ((c/s)^3)	0.31446E-02
Average Deviation (c/s)	0.17754
Skewness	0.31039 ± 0.31
Kurtosis	-0.17618 ± 0.62
Chi-Square	49.977 dof 62
Chi-Square Prob of constancy	0.86382
Kolm.-Smir. Prob of constancy	0.31303
RMS fractional variation	< 0.32991 (3 sigma)

Table 13.
Results from statistical analysis of X-ray spectrum lightcurve (obsID 00035019185)

Parameter	Obtained Value
Newbin Integration Time (s)	10.00
Interval Duration (s)	940.00
No. of Newbins	94
Average (c/s)	0.52987 ± 0.27E-01
Standard Deviation (c/s)	0.24238
Minimum (c/s)	0.12490
Maximum (c/s)	1.3770
Variance ((c/s)^2)	0.59187E-01 ± 0.87E-02
Expected Variance ((c/s)^2)	0.66850E-01 ± 0.98E-02
Third Moment ((c/s)^3)	0.79465E-02
Average Deviation (c/s)	0.19213
Skewness	0.15186 ± 0.25
Kurtosis	0.31080 ± 0.51
Chi-Square	82.902 dof 93
Chi-Square Prob of constancy	0.76411
Kolm.-Smir. Prob of constancy	0.47376
RMS fractional variation	< 0.38174 (3 sigma)

XRT Spectra
We present the results of the spectrum plots for all datasets in Figure 8. In each panel, the model fit appears as a continuous line over the data points (top), and the residuals are plotted below. The goodness test results are plotted in Figure 9, and the results for the model fit, measured flux, and uncertainties are shown in Tables 14 to 18.

Figure 8.
Model fit and residuals for all XRT datasets.

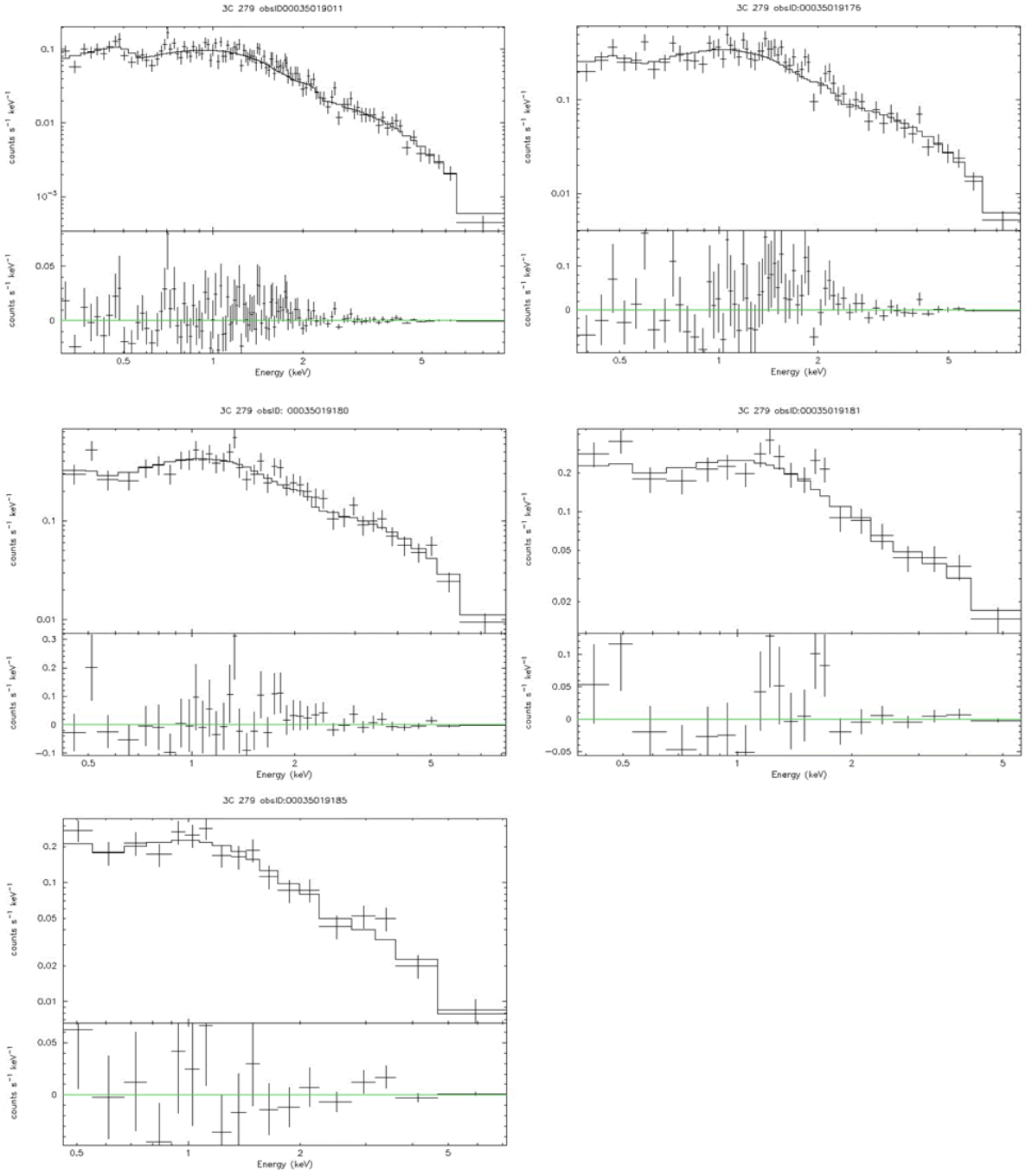

Figure 9.
Goodness test plots from all model fits.

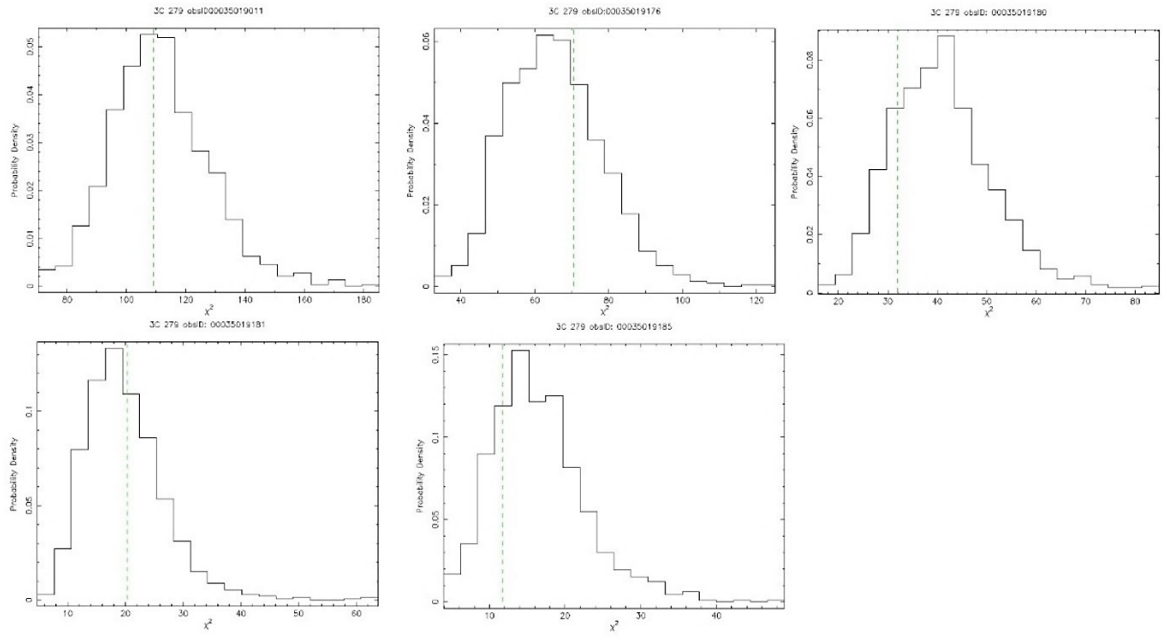

Table 14.
X-ray spectrum model results (obsID 00035019011)

Parameter	Obtained Value
N_H (cm^{-2})	Frozen at 0,022 × 10^{20}
Power Index	1,621 (−0,044 – +0,044)
Normalization Factor	1,937 (−0,066 – +0,066) × 10^{-3}
Flux$_0$,3–6 keV (log$_{10}$)	−10,841 (−0,019 – +0,018)
Flux$_0$,3–6 keV (erg cm^{-2} s^{-1})	1,44 (−0,060 – +0,063) × 10^{-11}
Luminosity (erg s^{-1})	1,657 (0,070 – 0,073) × 10^{46}
Goodness 1000 test (%)	46,90
Reduced χ^2	1,012

Table 15.
X-ray spectrum model results (obsID 00035019176)

Parameter	Obtained Value
N_H (cm^{-2})	Frozen at $0{,}022 \times 10^{20}$
Power Index	1,316 (−0,044 – +0,044)
Normalization Factor	5,209 (−0,280 – +0,278) × 10^{-3}
$Flux_0$,3–6 keV (log_{10})	−10,344 (−0,025 – +0,024)
$Flux_0$,3–6 keV (erg cm^{-2} s^{-1})	4,529 (−0,250 – +0,261) × 10^{-11}
Luminosity (erg s^{-1})	5,212 (0,290 – 0,302) × 10^{46}
Goodness 1000 test (%)	68,00
Reduced χ^2	1,104

Table 16.
X-ray spectrum model results (obsID 00035019180)

Parameter	Obtained Value
N_H (cm^{-2})	Frozen at $0{,}022 \times 10^{20}$
Power Index	1,177 (−0,081 – +0,082)
Normalization Factor	6,370 (−0,462 – +0,461) × 10^{-3}
$Flux_0$,3–6 keV (log_{10})	−10,194 (−0,032 – +0,036)
$Flux_0$,3–6 keV (erg cm^{-2} s^{-1})	6,397 (−0,530 – +0,471) × 10^{-11}
Luminosity (erg s^{-1})	7,362 (0,302 – 0,544) × 10^{46}
Goodness 1000 test (%)	19,10
Reduced χ^2	0,779

Table 17.
X-ray spectrum model results (obsID 00035019181)

Parameter	Obtained Value
N_H (cm^{-2})	Frozen at $0{,}022 \times 10^{20}$
Power Index	1,483 (−0,129 – +0,132)
Normalization Factor	3,844 (−0,358 – +0,355) × 10^{-3}
$Flux_0$,3–6 keV (log_{10})	−10,645 (−0,044 – +0,040)
$Flux_0$,3–6 keV (erg cm^{-2} s^{-1})	2,265 (−0,189 – +0,167) × 10^{-11}
Luminosity (erg s^{-1})	2,607 (0,027 – 0,193) × 10^{46}
Goodness 1000 test (%)	58,40
Reduced χ^2	0,969

Table 18.
X-ray spectrum model results (obsID 00035019185)

Parameter	Obtained Value
N_H (cm^{-2})	Frozen at $0{,}022 \times 10^{20}$
Power Index	1,506 (−0,144 – +0,149)
Normalization Factor	3,552 (−0,377 – +0,374) × 10^{-3}
$Flux_0$,3–6 keV (log_{10})	−10,642 (−0,048 – +0,044)
$Flux_0$,3–6 keV (erg cm^{-2} s^{-1})	2,280 (−0,231 – +0,252) × 10^{-11}
Luminosity (erg s^{-1})	2,640 (0,266 – 0,290) × 10^{46}
Goodness 1000 test (%)	22,30
Reduced χ^2	0,658

DISCUSSION

From our datasets we can see that, in observation date order, each subsequent dataset has less observing time than the one before. This was not intentional in the selection of the datasets; however, this can have an impact on the interpretation of our results, because the datasets that have longer observation durations also will have an increased S/N. This can clearly be seen in the UVOT results tables in the σ significance.

The fact that different UVOT observations also were done with different filters between them makes a combined analysis of the flux over datasets more difficult, since each filter will have different responses. Ideally, for our purposes, datasets taken with one filter should be compared to datasets utilizing the same filter.

The lightcurves and spectra plots from UVOT may also seem devoid of data at first glance considering that, for example, the dataset obsID:00035019011 was obtained from a 4 h observation window and one plot only contains one datapoint. However, this is due to the way the UVOT telescope operates in comparison to XRT; UVOT collects data in exposure-based images, meaning that each data point comes from an entire integration period rather than a continuous stream of detected photons analyzed individually, as is otherwise the case for XRT photon counting mode (Swift Team 2025). Thus, only one dataset (obsID:00035019011) produced a lightcurve with enough datapoints to observe a behavior across time during the observation window, where no significant variability in the observation window of about 4 h is displayed.

On the other hand, one dataset (obsID:00035019181) did not produce any lightcurve or spectrum plot for UVOT. It was downloaded and analyzed multiple times without success, so we attribute this to some type of information missing from the dataset which the pipeline requires to perform the plots. However, this dataset nor others presented further problems in the data reduction process.

Since XRT does not use filters but measures across the full available range of the telescope continuously (0.2–10 keV), comparisons between datasets in XRT are more relevant than those of UVOT in our analysis.

For the XRT datasets, we organized the datapoints in both the lightcurve and the spectrum files in order to be able to apply Gaussian statistics to the results. The χ^2 is the result of the comparison between the lightcurve and a constant count rate; the reduced χ^2 indicates a good agreement between the data and the model if the value is lower than 1. It is obtained by dividing χ^2 by the number of bins, and the probability of constancy indicates the probability of the source's flux emission being constant.

Since XRT measures each photon individually as it reaches the detector instead of over an integrated period of time, it is much more sensitive to changes in exposure time for each dataset, as we still need a minimum of 20 counts per bin to perform Gaussian statistics. This can be seen in the XRT lightcurves and spectra: plots that come from longer exposure windows have more datapoints and thus their statistics are more robust than those with fewer datapoints.

The flux energy range we chose to focus our analysis on (0.3–6 keV) was chosen from observing how each spectrum plot turned out on XRT for each dataset and selecting the minimum common values between them. That is, when removing the bad data as flagged by XSPEC for each spectrum, we chose the flux range that all datasets were able to measure without bad-quality flags. It is possible to assume that with longer observation windows across all datasets we could increase the higher end of the measured flux.

Given that we had a common flux range measured across all datasets, we decided to include the estimated luminosity in the final results.

We also performed a goodness test on each dataset, where XSPEC performs simulations of the data based on the current chosen model with its parameters and compares the statistical values calculated with those corresponding to the real measured data. In our case, we chose 1000 of these simulations.

From a goodness test, we can deduce that a high percentage result (close to 1) means that the observed test statistic is not extreme compared to the simulated ones; on the other hand, a lower percentage result (close to 0) means that the observed test statistic is more extreme than most of the simulated ones, suggesting that the observed data is unlikely under the null hypothesis, that is, it is a bad fit.

Our results for the goodness test can be seen in Figure 9 and in Tables 14 to 19.

It is evident from the goodness test also that the more datapoints we are able to analyze, the more confidence we have in the model. However, even though some of our model fits had low goodness values (obsID:00035019180, obsID:00035019185), these are the same datasets which resulted in a lower number of bins, which in turn comes from the short observation windows. In any case, the χ^2 analysis and, more so, our obtained values for the photon index in the power-law model range from 1.177 to 1.621, which is consistent with findings for the photon index across the same energy range in other studies. (Thekkoth 2023) reports ≈ 1.5, and (Giuliani 2008) reports ≈ 1.4 for the photon index.

The conversion from logarithmic flux to flux in $erg\ cm^{-2}\ s^{-1}$, used in the computation for luminosity, was calculated with:

$$F = 10^{F_{Log_{10}}}$$
$$\sigma_f = F \cdot ln(10) \cdot \sigma_{10^{F_{Log_{10}}}}$$

$$\sigma_f = F \cdot ln(10) \cdot \sigma_{10^{F_{Log_{10}}}}$$

Where:

- F is the flux in $erg\ cm^{-2}\ s^{-1}$
- $F_{Log_{10}}$ is the logarithmic flux
- $\sigma_{10^{F_{Log_{10}}}}$ is the uncertainty in the logarithmic flux
-

The formula to calculate luminosity L from flux F is given by:

$$L = 4\,\pi\,d^2\,F$$

Where:

- L is the luminosity in erg s^{-1}
- d is the distance to the object in cm
- F is the flux in erg cm^{-2} s^{-1}

The error propagation formula for the measured luminosity L is:

$$\frac{\sigma_L}{L} = \sqrt{\left(\frac{\sigma_d}{d}\right)^2 + \left(\frac{\sigma_F}{F}\right)^2}$$

This allowed us to analyze the luminosity output of the AGN before, during, and after the reported GRB event we desired to study.

We measured a significant increase in luminosity during the reported burst event, with a value of $\approx 5.212 \times 10^{46}\ erg\ s^{-1}$ (obsID: 00035019176) immediately before the peak of the event, rising to $\approx 7.362 \times 10^{46}\ erg\ s^{-1}$ during the highest emission (obsID: 00035019180), and a posterior decrease to $2.607 \times 10^{46}\ erg\ s^{-1}$ after the event (obsID: 00035019181), all within the range of 0.3–6 keV.

The dataset obsID: 00035019011, which had the longest exposure time, resulted in a measured luminosity of $1.657 \times 10^{46}\, erg\, s^{-1}$. Results for the luminosity in the soft-to-mid X-ray energy range in the literature for 3C-279 are consistent with our findings, as (Paliya 2015), (Beresnyak 2019), and others report luminosity levels of up to $\approx 10^{46}\, erg\, s^{-1}$ for increased activity states of this target.

Some researchers suggest that the peaks in activity of 3C-279 take several days to develop (Singh 2020), meaning that our dataset pertaining to immediately before the supposed peak of the event (obsID: 00035019180) may have been taken when the AGN was already in an active state. This interpretation is consistent with our measured luminosities; however, an increase–peak–decrease trend can still be observed when comparing the datasets.

Authors such as (Wang 2022) and (Wendel 2021) propose external inverse Compton scattering as one of the main mechanisms responsible for some of the GRB events Swift detects, first by BAT and then by UVOT and XRT, as increases in soft-to-medium X-ray activity (0.1–12 keV). This is consistent with the energy ranges and results presented in this report.

CONCLUSIONS

UVOT and XRT are excellent tools to analyze and characterize the behavior of transient events; however, particular consideration must be taken in the choice of target and the techniques applied, given that the telescope's instruments have different limitations and advantages.

UVOT uses filters and is designed to study low X-ray sources through integrated exposure frames, while XRT is aimed at studying mid-level X-ray sources and is able to analyze the full spectrum over this energy range.

Longer exposures with XRT will result in a more robust model for sources, but even with shorter observation windows, if enough datasets are considered, a reliable model can be proposed, as demonstrated in this report.

We successfully processed data from the XRT and UVOT instruments aboard the Swift telescope. We proposed a spectral model for the blazar 3C-279 that aligns with existing literature in the low-to-mid X-ray energy range, including flux and luminosity outputs. Additionally, we accurately measured an increase, peak, and subsequent decrease in the AGN's luminosity during a reported GRB event, with flux and luminosity magnitudes consistent with those found in the literature.

Suggestions for further research on the modeling and characterization of parameters from this AGN include:

- incorporating more datasets with long exposure windows for XRT,
- utilizing UVOT datasets with the same filter across multiple exposures, to enable the production of lightcurves with more datapoints,
- and performing simultaneous analyses of both instruments' data rather than treating them separately.
-

These improvements would allow for a more comprehensive understanding of the AGN's behavior during other reported GRB events.

BIBLIOGRAPHIC REFERENCES

Albert, J., Aliu, E., Anderhub, H., Antonelli, L.A., Antoranz, P., Backes, M. *et al.* (2008). Very-high-energy gamma rays from a distant quasar: how transparent is the universe? *Science*, 320 (5884), 1752–1754. https://doi.org/10.1126/science.1157087

Akiyama, K., Alberdi, A., Alef, W. *et al.* (2019). First M87 Event Horizon Telescope results VI: the shadow and mass of the central black hole. *Astrophys. J. Lett.*, 875 (1), L6. https://doi.org/10.3847/2041-8213/ab1141

Alston, W., Giustini, M. & Petrucci, P.O. (2022). The super-massive black hole close environment in active galactic nuclei. *arXiv preprint*, arXiv:2206.11790. https://arxiv.org/abs/2206.11790

Bellovary, J.M., Low, M.-M.M., McKernan, B. & Ford, K.E.S. (2016). Migration traps in disks around supermassive black holes. *Astrophys. J. Lett.*, 819 (2), L17. https://doi.org/10.3847/2041-8205/819/2/L17

Beresnyak, A.R., Istomin, Ya.N. & Pariev, V.I. (1997). Synchrotron emission from relativistic parsec-scale jets. *arXiv preprint*, arXiv:astro-ph/9704046. https://arxiv.org/abs/astro-ph/9704046

Blinov, D., Jorstad, S.G., Larionov, V.M. *et al.* (2021). Repeated pattern of gamma-ray flares in the light curve of the blazar 3C-279. *Mon. Not. R. Astron. Soc.*, 505 (3), 4616–4625. https://doi.org/10.1093/mnras/stab1484

Burrows, D.N., Hill, J.E., Nousek, J.A. *et al.* (2005). The Swift X-Ray Telescope. *Space Sci. Rev.*, 120 (3–4), 165–195. https://doi.org/10.1007/s11214-005-5097-2

Epstein-Martin, M., Tagawa, H., Haiman, Z. & Perna, R. (2025). Time-dependent models of AGN disks with radiation from embedded stellar-mass black holes. *arXiv preprint*, arXiv:2405.09380. https://arxiv.org/abs/2405.09380

Fabian, A.C. (2012). Observational evidence of active galactic nuclei feedback. *Annu. Rev. Astron. Astrophys.*, 50 (1), 455–489. https://doi.org/10.1146/annurev-astro-081811-125521

Fermi-LAT Collaboration (2010). A change in the optical polarization associated with a γ-ray flare in the blazar 3C-279. *Nature*, 463 (7283), 919–923. https://doi.org/10.1038/nature08841

Giuliani, A., D'Ammando, F., Vercellone, S. *et al.* (2008). AGILE observation of a gamma-ray flare from the blazar 3C-279. *Astron. Astrophys.*, 494 (2), 509–513. https://doi.org/10.1051/0004-6361:200810785

Hartman, R. C., Bertsch, D. L., Fichtel, C. E., et al. (1992). Detection of high-energy gamma radiation from quasar 3C 279 by the EGRET telescope on the Compton Gamma Ray Observatory. *Astrophysical Journal Letters,* 385, L1–L4. https://doi.org/10.1086/186263

Hayashida, M., Nalewajko, K., Madejski, G.M. *et al.* (2015). Rapid variability of blazar 3C-279 during flaring states in 2013–2014 with joint Fermi-LAT, NuSTAR, Swift, and ground-based multi-wavelength observations. *Astrophys. J.*, 807 (1), 79. https://doi.org/10.1088/0004-637X/807/1/79

HEASARC (2025). XSPEC manual. Available at: https://heasarc.gsfc.nasa.gov/xanadu/xspec/manual/XspecManual.html (Accessed 25 March 2025).

HEASARC (2025). WebPIMMS (W3PIMMS tool). Available at: https://heasarc.gsfc.nasa.gov/cgi-bin/Tools/w3pimms/w3pimms.pl (Accessed 25 March 2025).

HEASARC (2025). High Energy Astrophysics Science Archive Research Center (HEASARC). Available at: https://heasarc.gsfc.nasa.gov/cgi-bin/W3Browse/swift.pl (Accessed 26 March 2025).

NASA Swift Team (2025). Swift observatory: about. Available at: https://swift.gsfc.nasa.gov/about_swift/ (Accessed 26 March 2025).

NASA Swift Team (2025). Swift XRT point spread function (PSF). Available at: https://swift.gsfc.nasa.gov/proposals/tech_appd/swiftta_v17/node36.html (Accessed 25 March 2025).

NASA/IPAC Extragalactic Database (NED) (2025) 3C-279. Available at: https://ned.ipac.caltech.edu/byname?objname=3C279&hconst=67.8&omegam=0.308&omegav=0.692&wmap=4&corr_z=1 (Accessed 25 March 2025).

Padovani, P. (2023). A multi-wavelength view of active galactic nuclei with an emphasis on gamma-rays. *arXiv preprint*, arXiv:2302.12540. https://arxiv.org/abs/2302.12540

Paliya, V.S., Sahayanathan, S. & Stalin, C.S. (2015). Multi-wavelength observations of 3C-279 during the extremely bright gamma-ray flare in 2014 March–April. *Astrophys. J.*, 803 (1), 15. https://doi.org/10.1088/0004-637X/803/1/15

Prince, R. (2020). Broadband variability and correlation study of 3C-279 during flares of 2017–2018. *Astrophys. J.*, 890 (2), 164. https://doi.org/10.3847/1538-4357/ab6b1e

Rajguru *et al.* (2024). Accretion disc–jet decomposition from the optical–near infrared monitoring of Fermi blazars. *Mon. Not. R. Astron. Soc.*, 535 (4), 3595–3610. https://doi.org/10.1093/mnras/stae2608

Romoli, C., Zacharias, M., Meyer, M. *et al.* (2017). Observation of the extremely bright flare of the FSRQ 3C-279 with H.E.S.S. II. *arXiv preprint*, arXiv:1708.00882. https://arxiv.org/abs/1708.00882

Singh, K.K., Meintjes, P.J. & Ramamonjisoa, F.A. (2020). Understanding the giant gamma-ray outburst on June 16, 2015 from the blazar 3C-279. *Astrophys. Space Sci.*, 365 (2), 1–9. https://doi.org/10.1007/s10509-020-3746-2

Swift Team (2025). UVOT filters. Available at: https://www.swift.ac.uk/analysis/uvot/filters.php (Accessed 25 March 2025).

Thekkoth, A., Sahayanathan, S., Shah, Z., Paliya, V.S. & Ravikumar, C.D. (2023). Understanding the broad-band emission process of 3C-279 through long-term spectral analysis. *Mon. Not. R. Astron. Soc.*, 526 (4), 6364–6380. https://doi.org/10.1093/mnras/stad3094

Wang, G., Fan, J., Xiao, H. & Cai, J. (2022). Variability and spectral behavior of gamma-ray flares of 3C-279. *Publ. Astron. Soc. Pac.*, 134 (1040), 104101. https://doi.org/10.1088/1538-3873/ac98e0

Wendel, C., Shukla, A., & Mannheim, K. (2021). Pair cascades at the edge of the broad-line region shaping the gamma-ray spectrum of 3C-279. *Astrophys. J.*, 917 (1), 32. https://doi.org/10.3847/1538-4357/ac0a6e

European Southern Observatory (ESO) (2012). A stunning image of the galaxy NGC 6559 captured by the VLT. Available at: https://www.eso.org/public/italy/images/eso1229a/ (Accessed 2012).